Least-squares RTM: Theory and applications

Ping Wang*, Shouting Huang, and Ming Wang (CGG)

Abstract

We investigate how current least-squares reverse time migration (LSRTM) methods perform on subsalt images. First, we compare the formulation of data-domain vs. image-domain least-squares migration (LSM), as well as methods using single-iteration approximation vs. iterative inversion. Next, we examine the resulting subsalt images of several LSRTM methods applied on both synthetic and field data. Among our tests, we found image-domain single-iteration LSRTM methods, including an extension of Guitton's (2004) method in the curvelet domain, not only compensated for amplitude loss due to poor illumination caused by complex salt bodies but also produced subsalt images with fewer migration artifacts (i.e., noise) in the field data. By contrast, an iterative inversion method showed its potential for broadening bandwidth in the subsalt, but was less effective in reducing noise. Based on our understanding, we summarize the current state of LSRTM for subsalt imaging, especially between single-iteration and iterative LSRTM methods.

Introduction

We can consider recorded seismic data to be the results of forward modeling experiments through subsurface structures. To image the reflectivity of the subsurface, we need to reverse the forward wave-propagation effects with an inverse of the forward modeling operator. Reverse time migration (RTM), the state-of-the-art imaging technology for complex structures (Baysal et al., 1983; Etgen et al., 2009; Zhang and Zhang, 2009), uses an adjoint modeling operator to approximate the inverse of the forward modeling. However, the accuracy of this approximation is degraded by spatial aliasing, limited aperture, noise, and non-uniform illumination due to complex overburden (Claerbout, 1992). As a result, the RTM image may have migration artifacts with limited bandwidth and uneven amplitudes (Gray, 1997).

Least-squares migration (LSM) was proposed to approximate the inverse of the forward modeling operator. through either an iterative inversion (Tarantola, 1987; Schuster, 1993; Nemeth et al., 1999) or a single-iteration inversion (Hu et al., 2001; Rickett, 2003; Guitton, 2004; Lecomte, 2008). In recent years, least-squares reverse time migration (LSRTM) has attracted considerable attention (Wong et al., 2011; Dai et al., 2013; Zhang et al., 2013; Zeng et al., 2014). Improved image quality (both continuity and resolution), reductions in migration artifacts and noise, and better amplitudes are often cited as benefits of LSRTM; it is thus considered the next promising technology for subsalt imaging in the Gulf of Mexico (GOM) and other geologically complex regions.

Theory

LSM was first formulated in the data domain by Tarantola (1987). Data-domain LSM inverts for a reflectivity model, m, to fit the recorded data, d_0,

$$f_d(m) = \frac{1}{2}\|d_0 - Lm\|^2, \tag{1}$$

where f_d is the cost function to be minimized and L is the linearized Born modeling operator or demigration operator. Alternatively, LSM can be formulated in the image domain (Tang, 2008). Image-domain LSM inverts for a reflectivity model to fit the raw migrated image, $m_0 = L^T d_0$,

$$f_i(m) = \frac{1}{2}\|m_0 - L^T Lm\|^2, \tag{2}$$

where L^T is the migration operator. If $L^T L$ is invertible, the least-squares solution for both Equations 1 and 2 is unique and thus the same:

$$m = (L^T L)^{-1} L^T d_0, \tag{3}$$

where $L^T L$ is the so-called Hessian matrix, H. The key to LSM is to obtain the inverse of H; however, the computation and storage of H are not feasible for real 3D problems. Alternatively, different approximate solutions, including gradient-based iterative approaches (Schuster, 1993; Nemeth et al., 1999; Tang, 2008) and single-iteration approaches (Hu et al., 2001; Rickett, 2003; Guitton, 2004; Lecomte, 2008), have been pursued.

1. Iterative least-squares migration

Regardless of the invertibility of H, both Equations 1 and 2 can be iteratively solved by either steepest descent or conjugate gradient methods. The gradient for Equation 1 can be written as

$$g_d = L^T(d_0 - Lm), \tag{4}$$

while the gradient for Equation 2 can be written as

$$g_i = L^T L(m_0 - L^T Lm). \tag{5}$$

For one iteration of LSM, the computation of g_d in Equation 4 costs one Born modeling (i.e., demigration) and one migration; the computation of g_i in Equation 5 doubles this cost because of the cascade of modeling and migration operators. If ten iterations are needed for convergence, the costs of data-domain and image-domain iterative LSM are at a level of 20 and 40 migrations (although part of the computation for Born modeling and migration may be shared to save some costs), respectively. This can be computationally prohibitive for modern 3D marine streamer data that uses RTM extensively for model building as well as for final migrations that compute images with moderate- to high-frequency data.

2. Single-iteration least-squares migration

As discussed above, direct (Equation 3) or iterative (Equations 4 and 5) inversion methods are either impractical or expensive. The cost-reducing alternative is to approximate the Hessian matrix in a single iteration. Lecomte (2008) and Fletcher et al. (2016) proposed to obtain the Hessian matrix using point spread functions (PSFs). The PSF method computes the impulse response (Hessian) on a coarse grid (to reduce interference between PSFs) of scattered points. The Hessian for every image point is then obtained by interpolating between computed PSFs. LSM results are achieved by deconvolving computed PSFs from the raw migration image.

Guitton (2004) proposed to use non-stationary matching filters to approximate the inverse of the Hessian matrix in one iteration. In Guitton's approach, Born modeling (i.e., demigration) is first performed using the raw migration image, m_0, and the existing velocity field to derive synthetic data, $d_1 = Lm_0$, which are then remigrated to obtain a new image:

$$m_1 = L^T L m_0. \tag{6}$$

Next, non-stationary matching filters (or inverse Hessian filters), F, are found by minimizing the following cost function:

$$f(F) = \frac{1}{2}\|m_0 - Fm_1\|^2. \tag{7}$$

After obtaining F, the image-domain single-iteration LSM image can be written as:

$$m = Fm_0. \tag{8}$$

Guitton (2004) computes multi-coefficient matching filters in the spatial domain (Rickett et al., 2001). However, different events may have different illumination patterns. It is therefore desirable to decompose the input image for more accurate derivation of inverse Hessian filters.

3. Curvelet-domain Hessian filter (CHF)

The curvelet transform decomposes seismic events into different orientations and frequency scales. Utilizing the curvelet transform, we can extend the idea of a guided image filter proposed by He et al. (2013) to formulate a curvelet-domain Hessian filter (CHF). The cost function of the image-domain CHF can be written as

$$f(s) = \|C(m_0) - sC(m_1)\|^2 + \epsilon\|s\|^2, \tag{9}$$

where C is the curvelet transform operator, s is the matching filter, and ϵ is a weighting factor for Tikhonov regularization. The final output image is

$$m = C^{-1}(|s|C(m_0)), \tag{10}$$

where C^{-1} is the inverse curvelet transform operator and $|\ |$ is used to remove the phase and makes the matching filter a zero-phase filter. This CHF scheme can also be extended to the data domain (Khalil et al., 2016).

To compensate for offset-dependent illumination patterns, we further extend CHF to surface-offset gathers (SOGs) (Giboli et al., 2012):

$$f(s^{sog}) = \|C(m_0) - s^{sog}C(m_1^{sog})\|^2 + \epsilon\|s^{sog}\|^2, \tag{11}$$

$$m^{sog} = C^{-1}\left(|s^{sog}|C(m_0^{sog})\right). \tag{12}$$

Here, the same raw stacked image (m_0) is used to design the guided filter for each offset class. We note that the zero-phase filter is important for retaining event curvature.

Application to synthetic data

The SEAM I model contains realistic velocity contrasts with complex salt geometries that create a variety of subsalt illumination issues. It is an ideal synthetic data set for our initial evaluation of different LSRTM algorithms. For simplicity, we used the true velocity model and synthetic input data without surface multiples or added noise. To avoid the "inverse crime" (using the same modeling engine for both input and LSRTM), we modeled the input data using acoustic full-wave modeling instead of acoustic Born modeling, the demigration engine of all
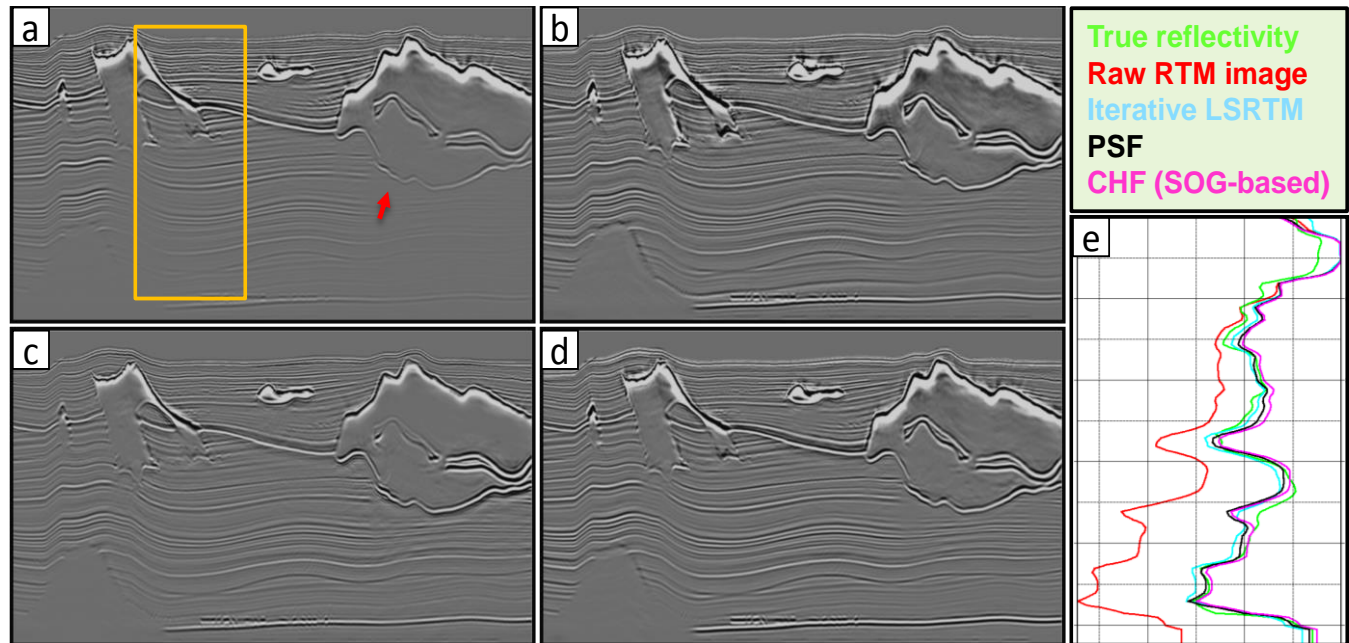

Figure 1: SEAM I synthetic study: (a) RTM image using forward modeled synthetic data; (b) iterative LSRTM image; (c) PSF deconvolution image; (d) CHF image; (e) amplitude decay curves (orange box in a) for images in Figures 1a-d.
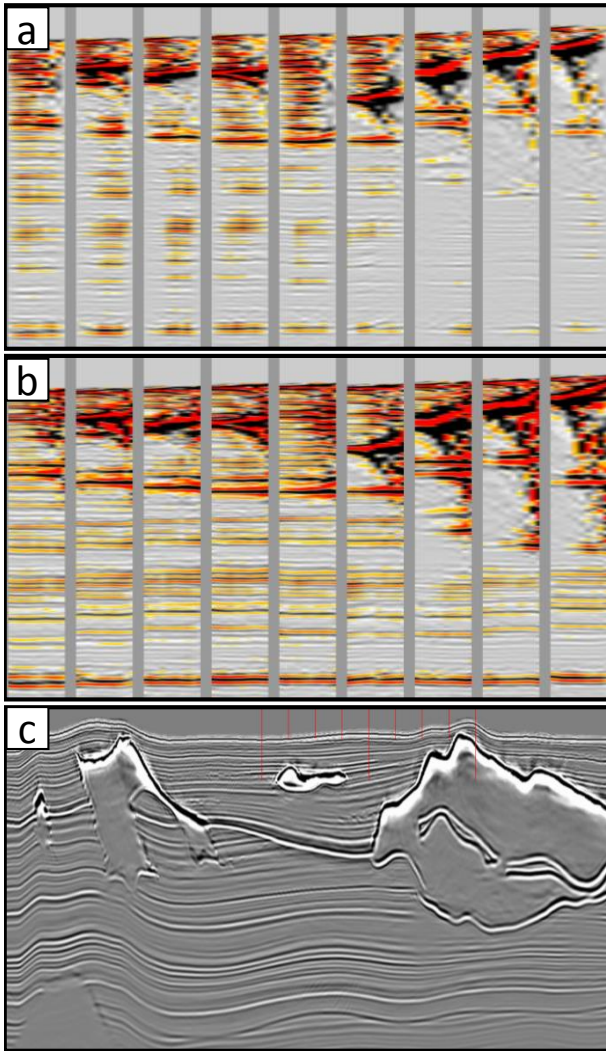
Figure 2: SEAM I synthetic study: (a) raw RTM surface-offset gathers; (b) LSRTM-CHF surface-offset gathers; (c) LSRTM-CHF stacked image. Red lines in (c) mark the gather locations in (a) and (b).

the LSRTM algorithms in this study. The modeling frequency is 10 Hz, the shot grid is 150 m × 150 m, while the receiver grid is 100 m × 100 m, and the maximum offset is 8 km in both inline and crossline directions.

Figure 1a is the raw RTM stack and Figure 1b shows the RTM stack after 20 iterations of iterative LSRTM. Figures 1c and 1d are the images after single-iteration LSRTM: PSF deconvolution and CHF, respectively. Overall, all three LSRTM methods produced similar stacks (Figures 1b, 1c, and 1d) with visually balanced amplitudes in the subsalt. To quantify the amplitude restoration, we compared the corresponding amplitude decay curves extracted from Figures 1b, 1c, and 1d with the input reflectivity (Figure 1e). Analogous to the RTM stacks, all three LSRTM methods produced similar amplitude decay curves as compared to the ground truth.

In the raw RTM SOGs (Figure 2a), we observe that the gathers on the left-hand side have weak amplitudes at near offsets but normal amplitudes at mid and far offsets.

This is due to the wavefields or raypaths contributing to the near offsets traveling through a small salt body in the overburden, while the raypaths of mid to far offsets undershoot the small salt body. This is not the case for the gathers on the right, which contain weak amplitudes across all offsets due to illumination loss from a much larger overburden salt body. As expected from LSRTM, gathers after CHF (Figure 2b) show balanced amplitudes across offsets as well as gather groups.

From these SEAM I subsalt synthetic LSRTM tests, we summarize the following:

1. All three LSRTM methods – iterative LSRTM, PSF, CHF – produced similar stack images and subsalt amplitude decay curves (Figure 1e) that matched the decay curve of the reflectivity model (the ground truth). However, under closer inspection, none of the three methods recovered events that are completely missing (red arrow in Figure 1a) on the raw RTM stack. Such events have very low or no illumination from the given acquisition and, therefore, cannot be modeled through Born modeling and restored by LSRTM.

2. Iterative LSRTM produced results comparable to those from the two single-iteration methods after ~20 iterations. This is consistent with Guitton's (2004) conclusion that a single-iteration LSRTM is a cost-effective alternative to iterative inversion.

3. As proposed by Fletcher et al. (2016), we computed multiple PSFs of interleaving grids to improve spatial sampling for interpolation while ensuring sufficient isolation of PSFs. This scheme was effective, but decreased the efficiency of the PSF approach. We also used salt damping to minimize deconvolution instability around salt bodies. In addition, we found a reweighting-based sparse deconvolution can be used to control noise (Sacchi, 1997).

4. In addition to its computational efficiency, CHF is appealing because it extends the illumination compensation from stack to SOGs, which potentially can be used for amplitude versus offset analysis and velocity model building.

We note that this test is not completely realistic because we did not include surface-related multiples or noise in the synthetic data, and we used the correct velocity model for the test. The reality and possibilities of LSRTM for subsalt imaging would be better answered using field data in a more realistic context, i.e., with an inevitably inaccurate velocity model and abundant noise from residual multiples.

GOM field data example

A wide-azimuth streamer data set from the Keathley Canyon area of the Gulf of Mexico was selected for the field data test. Although the area is known for well-defined salt geometries and overall good data quality, subsalt images in the area still suffer from uneven illumination, visible migration artifacts, and suboptimal resolution. The input data underwent typical preprocessing to remove noise, ghost energy, multiples, etc.
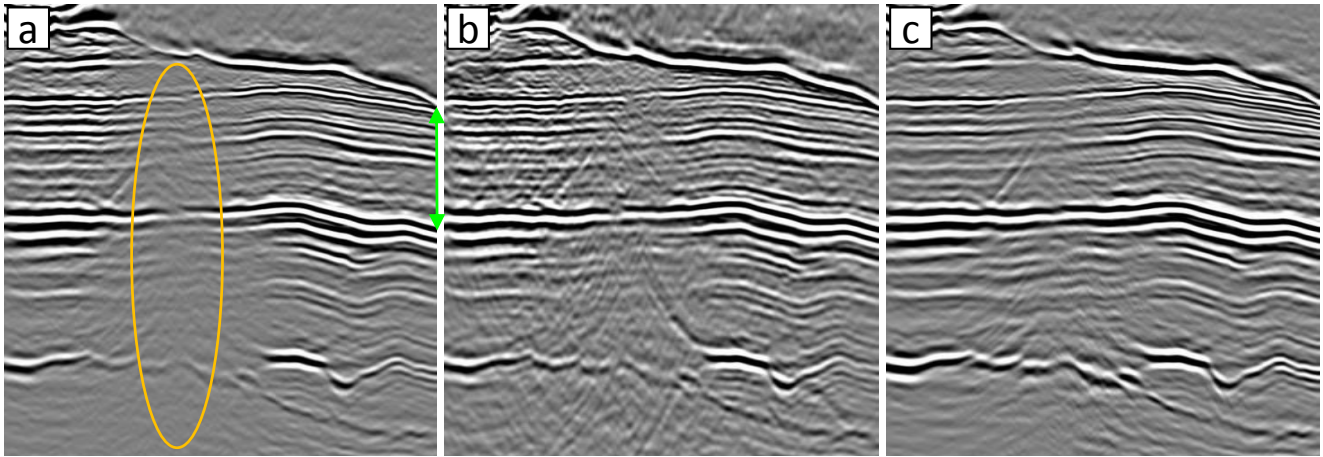
Figure 3: Gulf of Mexico field data example: (a) raw RTM image; (b) iterative LSRTM image (c) CHF image. Orange circle marks a weak amplitude zone due to illumination loss and green arrow marks the prospective Lower Tertiary interval.
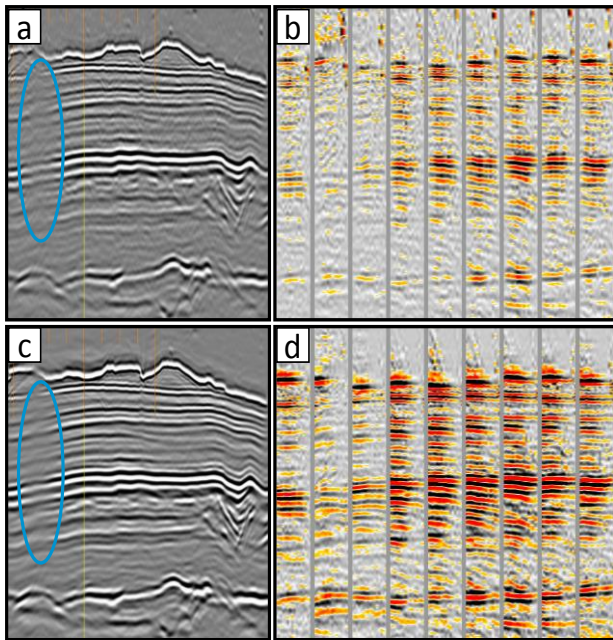

Figure 4: Gulf of Mexico field data example: (a) raw RTM stack image; (b) raw RTM surface-offset gathers; (c) LSRTM-CHF stack image; (d) LSRTM-CHF surface-offset gathers. Orange lines in (a) and (c) mark the gather locations in (b) and (d).

When compared to the raw RTM image (Figure 3a), iterative LSRTM (Figure 3b) produced more continuous subsalt events, particularly within the orange circle in Figure 3a. Similar to the results of the synthetic test, subsalt amplitudes in the field data are also more uniform after LSRTM. The resolution of the subsalt region in Figure 3b appears to be higher than the raw RTM stack (Figure 3a). The apparent higher resolution from the iterative LSRTM also boosted overall noise content. It is likely some of the noise was caused by over-fitting of some events that were present in the input data but cannot be correctly modeled by acoustic Born modeling. We stopped the test at the 10th iteration despite the presence of primary signal still in the data residual, because the noise level was increasing with the number of iterations. The CHF image (Figure 3c) also shows

balanced amplitudes and more continuous events in the subsalt. Unlike the iterative LSRTM, CHF did not noticeably alter the vertical resolution or frequency content. This is because we did not model the ghost when generating the demigration/migration image since the input data had already been deghosted, and we used a spiky source wavelet for both demigration and migration. As a result, the demigration/migration image (m_1) has similar frequency content to the raw RTM image (m_0). In addition, the design of CHF discourages over-boosting of frequency content with low signal-to-noise ratio (S/N) in the raw RTM image.

The quality of subsalt images is judged by many factors, including S/N, event and structural coherency, amplitude consistency, and resolution. Within the prospective Lower Tertiary interval (denoted by green up-down arrows in Figure 3a), CHF performed better in terms of noise suppression, while the iterative method yielded higher resolution but an increased noise level. Both methods were effective at balancing uneven amplitudes in the subsalt, as was also shown in the synthetic test.

Figure 4b shows raw RTM SOGs (m_0^{sog}) at locations indicated by the yellow lines in Figure 4a, and Figure 4d shows the same gathers after CHF (m^{sog}). We observed that SOGs after CHF have a higher S/N and more continuous subsalt events across all offsets while retaining the event curvatures. As counterintuitive as it seems, we may be able to use CHF SOGs to improve the velocity model, even though LSRTM assumes the velocity model is already correct. One possibility is to include CHF with key velocity model building steps, e.g., using the SOGs generated from CHF for better curvature picking and, in turn, better tomographic inversion. Of course, the computation of incorporating CHF in velocity estimation can be costly.

Figure 4c shows the stack image after CHF. The image has more balanced amplitudes and fewer migration artifacts compared to the raw stack image in Figure 4a. Note that events in the light blue circle were not well imaged by RTM, possibly due to velocity errors and/or inaccurate salt interpretation. As a result, CHF was unable to fully recover the amplitude dimming.

Discussion and conclusions

The performance of LSRTM is largely limited by the quality of the raw RTM image. It is very difficult, if not impossible, for any LSRTM method to recover subsalt events and structures that are completely missing on the raw RTM image. The absence of subsalt events on the raw RTM image can arise from a combination of factors, such as very low or no illumination, severe noise contamination, or an inaccurate velocity model. In subsalt imaging, a high-quality input data set not only provides better subsalt illumination and noise attenuation, it is also conducive to better velocity model derivation. Naturally, using a good input data set can increase the chances of success of LSRTM. A case in point is the advent of full-azimuth acquisition in the Gulf of Mexico, which has not only led to better subsalt illumination and noise cancellation, but has also produced higher-fidelity velocity models than would be obtained from a wide-azimuth data set.

LSRTM has shown promising results in subsalt imaging. It improves the amplitude response and reduces migration artifacts for both stacked images and gathers by compensating for irregular illumination due to complex overburdens and acquisition footprints. This can also potentially benefit subsalt quantitative interpretation and time-lapse imaging. Through additional synthetic and field data trials, the subsalt imaging community will continue to improve the algorithms and turn more of the possible benefits of LSRTM into reality.

Acknowledgments

References

Claerbout, J.F., 1992, Earth soundings analysis: Processing versus inversion: Blackwell Scientific Publications.

Baysal, E., D. Kosloff, and J. Sherwood, 1983, Reverse-time migration: Geophysics, **48**, 1514–1524. http://dx.doi.org/10.1190/1.1441434.

Dai, W., Y. Huang, and G. T. Schuster, 2013, Least-squares reverse time migration of marine data with frequency-selection encoding: Geophysics, **78**, no. 4, S233–S242. http://dx.doi.org/10.1190/geo2013-0003.1.

Etgen, J., S. Gray, and Y. Zhang, 2009, An overview of depth imaging in exploration geophysics: Geophysics, **74**, no. 6, WCA5–WCA17. http://dx.doi.org/10.1190/1.3223188.

Fletcher, R.P., D. Nichols, R. Bloor, and R.T. Coates, 2016, Least-squares migration — Data domain versus image domain using point spread functions, The Leading Edge, P159-162.

Giboli, M., R. Baina, L. Nicoletis, and B. Duquet, 2012, Reverse time migration surface offset gathers, Part 1: A new method to produce 'classical' common image gathers: 82nd Annual International Meeting, SEG, Expanded Abstracts, doi:10.1190/segam2012-1007.1.

Gray, S. H., 1997, True-amplitude seismic migration: A comparison of three approaches: Geophysics, **62**, no. 3, 929–936.

Guitton, A., 2004, Amplitude and kinematic corrections of migrated images for nonunitary imaging operators: Geophysics, **69**, no. 4, 1017–1024, http://dx.doi.org/10.1190/1.1778244.

He, K., J. Sun, and X. Tang, 2013, Guided image filtering: IEEE Transactions on Pattern Analysis and Machine Intelligence, Vol. 35, http://doi.ieeecomputersociety.org/10.1109/TPAMI.2012.213.

Hu, J., G. T. Schuster, and P. A. Valasek, 2001, Poststack migration deconvolution: Geophysics, **66**, no. 3, 939–952, http://dx.doi.org/10.1190/1.1444984.

Lecomte, I., 2008, Resolution and illumination analyses in PSDM: A ray-based approach: The Leading Edge, **27**, no. 5, 650–663, http://dx.doi.org/10.1190/1.2919584.

Nemeth, T., C. Wu, and G. T. Schuster, 1999, Least-squares migration of incomplete reflection data: Geophysics, **64**, no. 1, 208–221. http://dx.doi.org/10.1190/1.1444517.

Rickett, J., Guitton, A., and Gratwick, D., 2001, Adaptive multiple subtraction with non-stationary helical shaping filters: 63rd Annual Meeting, EAGE, Extended Abstracts, P167.

Rickett, J. E., 2003, Illumination-based normalization for wave equation depth migration: Geophysics, **68**, no. 4, 1371–1379, http://dx.doi.org/10.1190/1.1598130.

Sacchi, M. D., 1997, Reweighting strategies in seismic deconvolution: Geophys. J. Int., **129**, 651-656.

Schuster, G. T., 1993, Least-squares crosswell migration: 63rd Annual International Meeting, SEG, Expanded Abstracts, 110–113. http://dx.doi.org/10.1190/segam2012-1425.1.

Tang, Y., 2008, Wave-equation Hessian by phase encoding: 78th Annual International Meeting, SEG, Expanded Abstracts, 2201–2205.

Tarantola, A., 1987, Inverse problem theory: Methods for data fitting and model parameter estimation: Elsevier Science Publishing Company.

Wong, M., S. Ronen, and B. Biondi, 2011, Least-squares reverse-time migration/inversion for ocean bottom data: A case study: 81st Annual International Meeting, SEG, Expanded Abstracts, 2369–2373. http://dx.doi.org/10.1190/1.3627684.

Zeng, C., S. Dong, and B. Wang, 2014, Least-squares reverse time migration: inversion-based imaging toward true reflectivity: The Leading Edge, 33, 962–968. http://dx.doi.org/10.1190/tle33090962.1.

Zhang, Y. and H. Zhang, 2009, A stable TTI reverse time migration and its implementation, 79th Annual International Meeting, SEG, Extended Abstracts, 2794-2798. http://dx.doi.org/10.1190/1.3255429.

Zhang, Y., L. Duan, and Y. Xie, 2013, A stable and practical implementation of least-squares reverse time migration: 83rd Annual International Meeting, SEG, Expanded Abstracts, 3716–3720. http://dx.doi.org/10.1190/segam2013-0577.1.